

Rapid online learning and robust recall in a neuromorphic olfactory circuit

Nabil Imam¹, Thomas A. Cleland^{2*}

¹ Neuromorphic Computing Laboratory, Intel Labs, Santa Clara, CA 95054, USA.
nabil.imam@intel.com

² Computational Physiology Laboratory, Dept. Psychology, Cornell University, Ithaca, NY 14853, USA. tac29@cornell.edu.

* Correspondence to: Thomas A. Cleland, Dept. Psychology, Cornell University, Ithaca, NY 14853, USA. tac29@cornell.edu.

Abstract

The mammalian olfactory system learns new odors rapidly, exhibits negligible interference among odor memories, and identifies known odors under challenging conditions. The mechanisms by which it does so are unknown. We here present a general theory for odor learning and identification under noise in the olfactory system, and demonstrate its efficacy using a neuromorphic model of the olfactory bulb. As with biological olfaction, the spike timing-based algorithm utilizes distributed, event-driven computations and rapid online learning. Localized spike timing-dependent plasticity rules are employed iteratively over sequential gamma-frequency packets to construct odor representations from the activity of chemosensor arrays mounted in a wind tunnel. Learned odors then are reliably identified despite strong destructive interference. Noise resistance is enhanced by neuromodulation and contextual priming. Lifelong learning capabilities are enabled by adult neurogenesis. The algorithm is applicable to any signal identification problem in which high-dimensional signals are embedded in unknown backgrounds.

Introduction

The recognition of meaningful odors encountered within complex and unpredictable chemical environments constitutes the “hard problem” of olfactory neuroscience. Natural odors comprise mixtures of many different odorant molecules ¹; moreover, under natural conditions, different odors from many separate sources intermingle freely and, when inhaled together, chemically occlude one another in competition for odorant receptor binding sites ^{2, 3}. This occlusion substantially disrupts the primary sensory activation patterns that provide the basis for odor recognition. Under these challenging conditions, the mammalian olfactory system demonstrates levels of performance in signal restoration and identification currently unmatched by artificial systems ^{4, 5}.

The olfactory hard problem poses an ideal task for neuromorphic computing ^{6, 7}. Primary sensory representations of odor stimuli at steady state constitute intrinsically high-dimensional feature vectors, the dimensionality of which is defined by the number of receptor types expressed by the olfactory system ⁸. This number ranges from the hundreds to over 1000 in different mammalian species. Odor learning is rapid, and the recognition of learned odors becomes stronger and more specific over repeated presentations that contribute additional certainty ⁹⁻¹¹. Importantly, this learned identification of meaningful odors depends substantially on plastic circuitry in the mammalian main olfactory bulb (MOB) ¹¹⁻¹⁵.

Mechanistically, fast coherent oscillations in the gamma band (c. 30-80 Hz), which are intrinsic to MOB circuitry ^{16, 17}, phase-restrict the timing of action potentials evoked in activated principal neurons (mitral cells; MCs) ^{16, 18}. This property discretizes spiking output into gamma-breadth packets, enabling a robust within-packet phase precedence code ^{19, 20} by disambiguating phase-leading from phase-lagging spikes within the permissive epoch of each gamma cycle.

Recurrent activity loops in OB circuitry evince control systems architecture, implementing gain control in the superficial layers²¹⁻²³ and enabling attractor dynamics in the deeper network²⁴. Plastic synapses in the MOB support localized synaptic learning^{25, 26}, here instantiated as spike timing-dependent plasticity rules. The neuromodulatory tuning of MOB circuit properties²⁷⁻²⁹ here is leveraged as an optimization trajectory rather than a fixed state variable. Adult neurogenesis in the MOB, known to be required for odor learning and memory^{14, 15, 30, 31}, here provides indefinite capacity for lifelong learning through the permanent differentiation and replacement of plastic interneurons.

We present a neuromorphic network algorithm based on the neural circuitry of the external plexiform layer (EPL) of the mammalian OB and implemented on the Intel Loihi neuromorphic system³². By training and testing the model EPL network with chemosensor array data⁵, we show that this network rapidly learns odor representations and then can robustly identify these learned odors under high levels of destructive interference, outperforming multiple contemporary statistical techniques. We further conclude that representational learning is critical not simply for odor identification per se, but for the effectiveness of source separation and signal restoration under noise on which this identification depends.

Results

Model architecture

The design of the model network was based on the circuitry and computational properties of the mammalian MOB, optimized for efficient implementation as a spiking network on the Loihi chip. In particular, we instantiated some core principles of MOB computation that we have hypothesized for the biological system^{8, 17, 19, 33, 34} but which remain controversial, such as (1)

the dynamically acquired, learning-dependent topology of the lateral inhibitory network of the EPL, (2) the importance of gamma-discretized spike timing-based computation in the EPL, (3) the principle that MCs deliver excitation to granule cell interneurons (GCs) irrespective of distance, whereas GCs effectively inhibit MCs only when synaptically proximal to the MC soma, and only via GC spiking, (4) the principle that this inhibition of MCs by GCs predominantly manifests as delays in MC spike times on the gamma timescale, (5) the principle that these fine-timescale EPL computations do not meaningfully influence the coarse-timescale computations of the glomerular layer, (6) the principle that only a minority of principal neurons participate in gamma dynamics during any given stimulus presentation, (7) the permanent differentiation of GCs by the process of odor learning, and the consequent need for replacement by adult neurogenesis, and (8) the utility of treating neuromodulation as an optimization trajectory rather than as a stationary state.

Like the mammalian MOB, the neuromorphic model network is intrinsically columnar (Figure 1a). Each column comprises a single MC principal neuron as well as up to 50 inhibitory GC interneurons, coupled by moderately sparse intercolumnar excitatory synapses (connection probability = 0.2) and local (intracolumnar) inhibitory synapses. We activated the MCs of a 72-column EPL network using data drawn from an array of 72 metal oxide gas sensor (MOS) elements spatially distributed across the full 1.2 m breadth of a wind tunnel ⁵ (Figure 1b). In all cases, sensor array responses drawn from a common point in time were presented to the EPL network for training or testing. That is, individual odor presentations (“sniffs”) comprised steady-state feature vectors in which the pattern of amplitudes across vector elements reflected odor quality as well as sampling error arising from plume turbulence.

The EPL network is intrinsically oscillogenic in the gamma band (30-80 Hz)^{17,35}, and MC action potentials are statistically phase-constrained with respect to these local oscillations^{16,18}. In our EPL network, MC spikes were constrained in time by an ongoing network oscillation with alternating permissive and inhibitory epochs reflecting the periodic GABAergic inhibition of the OB gamma cycle^{33,35} (Figure 1c). Sensory integration and MC spiking were enabled only during permissive epochs, whereas inhibitory epochs reset and held the activation of all MCs at zero. Therefore, in the absence of learning, and given stationary sensor input, the temporal patterning of spikes evoked by a given odor directly reflected sensor activation levels – stronger excitation evoked correspondingly earlier spikes – and was repeated across successive gamma cycles (Figure 1c). Different odors evoked correspondingly different spatiotemporal spike patterns across the MC population, thereby generating a phase code, or precedence code, on the gamma timescale. After learning, GC feedback in each gamma cycle iteratively modified MC spike timing. Model output then was interpreted as an evolving series of representations, in which each successive representation consisted of the spatiotemporal pattern of MC spikes across the network delivered within the permissive epoch of a given gamma cycle. Each of these representations was recorded as a set of spikes, with each spike defined by the identity of the active MC and the spike latency with respect to the onset of that permissive epoch. These sets then were classified based on their similarities to previously learned representations. Five gamma cycles were embedded within each odor presentation (“sniff”).

Excitatory plasticity determines GC receptive fields

Each gamma-constrained array of MC action potentials, in addition to serving as network output, also drove its complement of postsynaptic GCs across the network. During learning, the

synaptic weights between MCs and GCs were systematically modified by experience. GCs were modeled as single-compartment neurons that accumulated excitatory synaptic inputs from their widely distributed presynaptic MCs. Upon reaching threshold, they generated spike events that inhibited their local postsynaptic MC in the subsequent gamma cycle.

GC spiking also initiated excitatory synaptic plasticity. Specifically, GCs learned to respond to higher-order stimulus features by becoming selective for specific combinations of MC spiking activity. To do this, we implemented a spike timing-dependent plasticity (STDP) rule that learned these input combinations in terms of a spike phase precedence coding metric on the gamma timescale ¹⁹. Under initial conditions, GCs required moderately synchronous spike inputs from several presynaptic MCs in order to evoke an action potential. Classical STDP most powerfully strengthens the synaptic weights of synapses mediating presynaptic spikes that immediately precede a postsynaptic spike; we implemented this principle with a heterosynaptic STDP rule that strengthened these synapses and weakened all other incoming synapses, including those in which the presynaptic MC spiked at other times or not at all (Figure 2a). Accordingly, spiking GCs ultimately learned a fixed dependency on the synchronous firing of a set of k MC inputs, with inputs from other MCs decaying to zero (effectively a “ k winners take all” learning rule). Consequently, at the end of the training period, the response to each trained odorant evoked a distributed ensemble of GCs tuned to a diversity of stimulus-specific higher-order correlation patterns (Figure 2b). Importantly, the pattern of inhibition across columns was governed by this excitatory synaptic plasticity, because all inhibitory synapses were within-column by design (Figure 1a).

Inhibitory plasticity constructs odor memories

Spikes evoked by GC interneurons delivered synaptic inhibition onto the MC of their local column. As proposed for the biological system, the weights of GC-mediated inhibitory inputs regulated the timing of MC spikes within the permissive phase of the gamma cycle, with stronger weights imposing greater MC spike time delays within each gamma cycle^{33, 34, 36}. In the neuromorphic system, a GC spike blocked the generation of a spike on its follower MC for a period of time corresponding to the inhibitory synaptic weight. During odor learning, the durations of GC spike-evoked inhibitory windows were iteratively modified until the release of inhibition on the MC soma coincided with a threshold crossing in the MC apical dendrite resulting from integrated sensory input (Figure 2c). During testing, the end of the GC inhibitory window permitted the MC to fire, and evoked a rebound spike in the MC even in the absence of sufficient apical dendritic input. Synaptic inputs from multiple local GCs onto a common MC were applied independently, thereby enabling a larger and more diverse range of higher-order GC receptive fields to inhibit that MC.

This inhibitory plasticity rule enables the EPL network to learn the timing relationships between MC spikes in response to a given odor stimulus. Consequently, because relative spike times signify MC activation levels, the network effectively learns the specific ratiometric pattern of activation levels among MCs that characterizes a given odor. This spatiotemporal basis for odor representation enables a substantially greater memory capacity than would be possible with spatial patterning alone; for example, two odors that activate the same population of MCs, but at different relative levels, can readily be distinguished by the trained network. Moreover, this spike timing-based metric for relational encoding, coupled with odor-specific profiles of feedback inhibition, renders these memory states as attractors, enabling incoming stimuli to be

correctly classified by the trained network despite surprisingly high degrees of destructive interference.

Odor learning enables identification of occluded stimuli

We first trained the 72-column network on the odorant toluene in one shot (i.e., one sniff, enabling learning over five gamma cycles), and then tested the response of the network to presentations of toluene contaminated with destructive interference. To generate this interference, we entirely replaced a proportion P of the sensory inputs with random values (*impulse noise*, $P = 0.6$ unless otherwise indicated) to represent strong and unpredictable receptor occlusion through simultaneous activation or inhibition by other ambient odorants. In a naïve network, the presentation of occluded toluene yielded an essentially stationary and uninformative representation (Figure 3a). However, in the trained network, the spiking activity generated by occluded toluene was attracted over the five gamma cycles toward the previously learned toluene representation, enabling clear identification of the occluded unknown (Figure 3b-e).

As hypothesized for the biological olfactory bulb, odor learning in the network induces the permanent differentiation of granule cells that thereby become selective for higher-order feature combinations that are relatively diagnostic of the learned odor³⁷ (Figure 2b). We tested whether increased allocations of GCs, enabling each MC to be inhibited by a broader selection of feature combinations, would improve odor learning and identification under noise. We found that increasing the number of undifferentiated GCs per column improved the robustness of signal restoration, increasing the similarity of the occluded signal to the learned representation after five gamma cycles (Figure 3f). Nevertheless, we limited our simulations to five GCs per trained

odorant and five gamma cycles per sniff in order to avoid ceiling effects and thereby better reveal the variables of greatest interest.

Adult neurogenesis enables lifelong learning

This learning algorithm irreversibly consumes GCs. Each odor memory is associated with a distributed population of differentiated GCs tuned to its complex diagnostic features; such GCs may or may not be employed in multiple odor representations depending on odor similarity and the values of k . Fully differentiated, mature GCs do not undergo further plasticity and hence are protected from catastrophic interference^{38,39}. The learning of successively presented new odorants, however, would be increasingly handicapped by the declining pool of undifferentiated GCs (Figure 3f). The competition among distinct new odorants can be substantially reduced by sparser initial MC→GC connectivity and higher numbers of GCs, among other parameters³⁷; however, genuine lifelong learning in such a system requires a steady source of undifferentiated GCs. Exactly this resource is provided to the mammalian olfactory system by constitutive adult neurogenesis. We propose that the critical role of adult neurogenesis in odor learning^{14,15,30,31,40} be interpreted in this light.

In the present model, constitutive adult neurogenesis was simulated by configuring a new set of five GCs in every column after each successively learned odor stimulus. Hence, training a 72-column network on ten odors yielded a network with 3600 differentiated GCs. New GCs each received initial synaptic connections from a randomly selected 20% of the MCs across the network, and delivered inhibition onto their cocolumnar MC.

Online learning of multiple representations

We then trained the 72-column network sequentially with all ten odorants in the dataset⁵, using both one-shot and ten-shot training regimens for each odor. In both cases, the network was trained on one odor first, followed by a second odor, then by a third, until all ten odors had been learned. Similar results were obtained irrespective of the order in which the ten odorants were trained. A set of new, undifferentiated GCs was added to the network after each odor was learned, reflecting the effects of adult neurogenesis. Critically, subsequent odor training did not disrupt the memories of previously learned odors; that is, the EPL network supports robust online learning, and is resistant to catastrophic forgetting. This capacity for online learning is essential for memory formation under natural conditions, as well as for continuous device operation in the field; in either case, new signals of potential significance may be encountered at unpredictable times, and must be incorporated nondestructively into an existing knowledge base.

Training was conducted under relatively low-noise conditions, following the principle that the acquisition of a strong odor memory occurs when the odor is clearly discernable and associated with some multimodal consequence. Specifically, one-shot learning utilized a single sample from the sensor array responses to a given odorant in the wind tunnel (sniff; 5 gamma cycles; Figure 1b). For ten-shot learning, per-trial learning rates were reduced and samples were drawn from timepoints spaced one second apart in the wind tunnel dataset; consequently, the ten sensor array responses to each odor differed from one another owing to the dynamics of the odor plume. We then measured the performance of these trained networks in response to presentations of impulse noise-corrupted odor stimuli.

During testing, sensor-evoked activity patterns generated by strongly occluded odor stimuli ($P = 0.6$) were attracted specifically towards the learned representation of the corresponding odor

(Figure 4a-c). Notably, the network was able to rapidly identify occluded instances of all ten odors within five gamma cycles whether trained using one-shot learning (Figure 4d) or via progressive learning over ten wind-tunnel samples separated in time (Figure 4e), and could identify odors affected by different degrees of occlusion (Figure 4f). An odor was considered identified when the spatiotemporal pattern of its evoked spiking activity exceeded a Jaccard similarity⁴¹ of 0.75 to one of the network's learned representations.

Neuromodulation and cortical priming improve performance

Neuromodulators like acetylcholine and noradrenaline generate powerful effects on stimulus representations and plasticity in multiple sensory systems including olfaction. Traditionally, they are treated as state variables that may sharpen representations, gate learning, or bias a network towards one source of input or another⁴²⁻⁴⁴. We instead modeled neuromodulatory effects as a dynamic search trajectory. Specifically, as the neuromodulator is released in response to active olfactory investigation (sampling), the local concentration around effector neurons and synapses rises over the course of successive sniffs, potentially enabling the most effective of the transient neuromodulatory states along that trajectory to govern the outcome of the stimulus identification process. We implemented a gradual reduction in the mean GC spiking threshold over the course of five sniffs of a corrupted odor signal, reflecting a concomitant increase in neuromodulator efficacy, and used the greatest of the five similarity values measured in the last gamma cycle within each sniff to classify the test odorant. Importantly, under very high noise conditions, each of the five “neuromodulatory” states performed best for some of the test odors and noise instantiations, indicating that a trajectory across a range of neuromodulatory states could yield superior classification performance

compared to any single state. Indeed, this strategy yielded a substantial improvement in classification performance at very high levels of impulse noise, approximately doubling classification performance at $P = 0.8$ (Figure 4f).

In the biological system, olfactory bulb activity patterns resembling those evoked by a specific odor can be evoked by contextual priming that is predictive of the arrival of that odor⁴⁵. We modeled this as a priming effect exerted by ascending piriform cortical neurons that synaptically excite GCs in olfactory bulb⁴⁶. Specifically, we presented the network with odor samples at an extreme level of destructive interference ($P = 0.9$) that largely precluded correct classification under default conditions (Figure 4f). When a fraction of the population of GCs normally activated by the presented odor were primed by lowering their spike thresholds, classification performance improved dramatically, to a degree corresponding to the fraction of primed GCs (Figure 4g). That is, even a weak prior expectation of an incoming odor stimulus suffices to draw an extremely occluded odor signal out of the noise and into the attractor.

Classification performance of the neuromorphic model

To evaluate the performance of the EPL model, we compared its classification performance to the performance of multiple conventional signal processing techniques: a median filter (MF), a total variation filter (TVF), principal components analysis (PCA), and a seven-layer deep autoencoder (DAE). Specifically, following training, we averaged the classification performance of each method across 100 different occluded presentations of each odor, with the occlusion level for each sample randomly and uniformly selected from the range $P = [0.2, 0.8]$, for a total of 1000 test samples. Incorrect classifications and failures to classify both were scored as failures.

The neuromorphic EPL substantially outperformed MF, TVF, and PCA, and also outperformed the DAE for one-shot learning, in which the training set contained no information about the distribution of error that would arise during testing owing to impulse noise (Figure 5a). To improve the DAE performance, we then trained it with 500 to 7000 samples of each of the ten odorants, with each sample independently occluded by impulse noise randomly and uniformly selected from the range $P = [0.2, 0.8]$, thereby matching the statistics of the subsequently presented test samples. Under this training regimen, the deep network required 3000 samples per odorant to achieve the classification performance that the EPL model achieved with 1 sample per odorant (Figure 5b). We then tested the online learning capacities of the two networks, in which the presentations of different odorants during training were sequential rather than uniformly interspersed. After training both networks to recognize toluene, both the EPL and the DAE exhibited high classification performance. However, after subsequent training to recognize acetone, the DAE lost its ability to recognize toluene, whereas the EPL network recognized both odors with high fidelity (Figure 5c-d). Furthermore, as illustrated above, the performance of the neuromorphic EPL could be further enhanced by the provision of additional GCs (Figure 3f) and the inclusion of additional gamma cycles per sniff.

Summary

We demonstrate that a simplified network model, based on the architecture and dynamics of the mammalian olfactory bulb ³³ and instantiated in the Loihi neuromorphic system ³², can support rapid online learning and powerful signal restoration of odor inputs that are strongly occluded by contaminants, thereby directly addressing the “hard problem” of olfaction. These results evince powerful computational features of the early olfactory network that, together with

mechanistic models and experimental data, present a coherent general framework for understanding mammalian olfaction as well as improving the performance of artificial chemosensory systems. Moreover, this framework is equally applicable to other steady-state signal identification problems in which higher-dimensional patterns without meaningful lower-dimensional internal structure are embedded in highly interfering backgrounds.

Acknowledgments

Funding

Supported by NIDCD R01 grants DC014701 and DC014367 to TAC.

Author Contributions

TAC conceived the original algorithm. NI instantiated the algorithm and enhanced the learning rules, and subsequently ported it to Loihi. TAC and NI wrote the manuscript.

Data and Materials Availability

The gas sensor dataset utilized is freely available from the UCI Machine Learning database (<http://archive.ics.uci.edu/ml/datasets/gas+sensor+arrays+in+open+sampling+settings>).

Methods

Odorant sampling

Sensory input to the model was generated from a dataset of the responses of 72 metal-oxide based chemical sensors distributed across a wind tunnel⁵. Specifically, the tunnel was 1.2 m wide x 0.4 m tall x 2.5 m long, with the sensors deployed in nine modules, each with eight different sensors, distributed across the full 1.2 m width of the tunnel at a location 1.18 m from the inlet (Figure 1b). The nominal wind speed was 0.21 m s⁻¹, induced by running the exhaust fan at 3900 rpm, and the tunnel’s heater voltage was set to 500 V. The turbulence of the plume resulted in local concentration-based variance in the ten samples used to train the network in the ten-shot learning case; these samples were drawn from timepoints one second apart (i.e., a total span of nine seconds). The turbulent plume shown in Figure 1b is illustrative only; actual distribution maps of local concentrations in the plume, along with full details of the wind tunnel configuration, are provided in⁵.

Ten different odorants were delivered in the gas phase to the sensor array: acetone, acetaldehyde, ammonia, butanol, ethylene, methane, methanol, carbon monoxide, benzene, and toluene⁵. Each sensor’s range of possible responses was discretized into 16 levels of activation (integer values of 0 to 15) and the resulting values were composed into a 72-dimensional sensor activity vector, which then was sparsened by setting the smallest 50% of the values to zero. Accordingly, each odorant sample (“sniff”) presented to the EPL network comprised a single 72-element sensor vector drawn from a single point in time and presented as steady state. The OB EPL model therefore was instantiated with 72 columns, such that each column received afferent excitation proportional to the activation level of one sensor. Each model OB column comprised one principal neuron (MC) and initially five GC interneurons (for a total of 360 across all

columns), though the number of GCs per column rose as high as 50 in the most highly trained models described herein (see *Adult neurogenesis* section). MCs projected axons globally across all columns without respect to any measure of distance, and formed excitatory synapses onto GCs with a probability of 0.2 (20%). Each GC, in turn, synaptically inhibited the MC within its column with a probability of unity (100%). GCs did not inhibit MCs from other columns.

Intrinsic gamma and theta dynamics

In the biological system, the profile of spike times across MCs is proposed to reflect a phase precedence code with respect to the emergent gamma-band field potential oscillations generated in the olfactory system. Spike timing-based coding metrics are known to offer considerable speed and efficiency advantages⁴⁷⁻⁵¹; however, they require computational infrastructure in the brain to realize these benefits. Fast oscillations in the local field potential are indicative of broad activity coherence across a synaptically coordinated ensemble of neurons, and thereby serve as temporal reference frames within which spike times in these neurons can be regulated and decoded. Accordingly, these reference frames are essential components of the biological system's computational capacities.

In the OB, gamma oscillations emerge from interactions of the subthreshold oscillations of MCs with the network dynamics of the EPL (PRING dynamics;³³). For present purposes, the importance of these oscillations was twofold: (1) MC spike phases with respect to the gamma-band oscillations serve as the model's most informative output, and (2) by considering each oscillation as embedding a distinct, interpretable representation, repeated oscillations enable the network to iteratively approach a learned state based on stationary sensory input. Notably, *in vivo*, piriform cortical pyramidal neurons are selectively activated by convergent, synchronous

MC spikes ⁵², and established neural learning rules are in principle capable of reading such a coincidence-based metric ⁵³. Because MC spike times can be altered on the gamma timescale by synaptic inhibition from GCs, and their spike times in turn alter the responsivity of GCs, these lateral inhibitory interactions can iteratively modify the information exported from the OB. In the neuromorphic EPL, each MC periodically switched between two states to establish the basic gamma oscillatory cycle. These two states were an active state in which the MC integrated sensory input and generated spikes (*permissive epoch*) and an inactive state in which the excitation level of the MC was held at zero, preventing sensory integration and spike generation (*inhibitory epoch*; Figure 1c). The effects of the plastic lateral inhibitory weights from GCs were applied on top of this temporal framework (see *Inhibitory synaptic plasticity* section). The correspondence with real time is arbitrary and hence is measured in timesteps (ts) directly.

A second, slower, sampling cycle was used to regulate odor sampling. This cycle is analogous to theta-band oscillations in the OB, which are driven primarily by respiratory sampling (sniffing) behaviors but also by coupling with other brain structures during certain behavioral epochs. Each sampling cycle (“sniff”) consisted of a steady-state presentation of sensory input and five gamma cycles of network activity. The number of gamma cycles per sampling cycle can be arbitrarily determined in order to regulate how much sequential, iterative processing is applied to each sensory sample, but was held at five for all experiments herein.

Mitral cells

Each MC was modeled by two compartments – an apical dendrite (AD) compartment that integrated sensor input and generated “spike initiation” events when an activation threshold was crossed, and a soma compartment that was excited by spike initiation events in the AD

compartment and synaptically inhibited by spikes evoked in cocolumnar GCs. The soma compartment propagated the AD-initiated spike as an MC action potential after release from GC inhibition (see Methods). Distinguishing between these two compartments facilitated management of the two input sources and their different coding metrics, and reflected the biophysical segregation between the mass-action excitation of MC dendritic arbors and the intrinsic regulation of MC spike timing governed by the gamma-band oscillatory dynamics of the OB external plexiform layer ³³.

Sensor activation levels were delivered to the AD compartment of the corresponding column, which integrated the input during each permissive epoch of gamma. When the integrated excitation exceeded threshold, a spike initiation event was generated and communicated to the soma. Stronger inputs resulted in more rapid integration and correspondingly earlier event times. After generating an event, the AD entered a refractory period for the duration of that permissive epoch.

A spike initiation event in the AD generated a unit level of excitation (+1) in the soma compartment for the remainder of the permissive epoch. This excitation state caused the MC soma to propagate the spike as soon as it was sufficiently free of lateral inhibition received from its cocolumnar GCs. Accordingly, the main effect of GC synaptic inhibition was to modulate MC spike times with respect to the gamma cycle. The resulting MC spikes constituted model output, and also were delivered to its postsynaptic GCs.

During the first gamma cycle following odor presentation, when GC inhibition was not yet active, the soma immediately propagated the MC spike initiated in the AD. After propagating a spike, the soma entered a refractory period for the duration of the permissive epoch; consequently, an MC could spike a maximum of once per gamma cycle. At the end of the

permissive epoch, both the AD and soma compartments were reset to zero for the duration of the inhibitory epoch.

Granule cells

GCs were modeled as single-compartment neurons,

$$V = \sum_k w_k s_k \quad (1)$$

in which V indicates the excitation level of the GC, w_k represents the excitatory synaptic weight from a presynaptic MC soma k , and k was summed over all presynaptic MCs. The boolean term s_k denotes a spike at the k -th presynaptic MC soma; s_k equals 0 at all times except for the d -th timestep following a spike in the k -th MC soma, when it was set to 1. Accordingly, d denotes a delay in the receipt of synaptic excitation by a GC following an MC spike. This delay d was randomly determined, synapse-specific, and stable (i.e., not plastic); it reflects heterogeneities in spike propagation delays in the biological system and served to delay GC excitation such that GC spikes were evoked within the inhibitory epoch of gamma.

A spike in an MC soma k that was presynaptic to a given GC excited that GC in proportion to its synaptic weight w_k . Once GC excitation rose above a threshold θ_{GC} , the GC generated a spike and reset its excitation level to zero. Following a spike, the GC entered a refractory period for 20 timesteps, ensuring that only one spike could be initiated in a given GC per gamma cycle. In general, convergent excitation from multiple MCs was required for GC spike initiation.

Excitatory synaptic plasticity

The weights of MC-to-GC synapses were initialized to a value of w_e . Following an asymmetric spike timing-dependent plasticity rule, these synaptic weights were modified during training following a spike in the postsynaptic GC. Specifically, synapses in which the

presynaptic MC spike preceded the postsynaptic GC spike by 1 timestep were potentiated by a constant value of δ_p whereas all other synapses were depressed by a constant value of δ_d . In the present study, we set δ_p to $0.05w_e$ and δ_d to $0.2w_e$ for one-shot training, and set both values to $0.005w_e$ for ten-shot training. Additionally, following ten-shot training, synapses that were depressed below a threshold weight of w_e were removed. GC spiking thresholds were set to $6w_e$.

The overall effect of this rule was to develop sparse and selective higher-order receptive fields for each GC, a process termed differentiation. Specifically, repeated coincidences of the same MC spikes resulted in repeated potentiation of the corresponding synapses, whereas synapses of other MCs underwent repeated depression. Individual excitatory synaptic weights were capped at a value of $1.25w_e$, ensuring that the spiking of differentiated GCs remained sensitive to coincident activity in a particular ensemble of MCs, the number of which constituted the order of the GC receptive field. By this process, odor learning transformed the relatively broad initial receptive field of a GC into a highly selective one of order M. These higher-order receptive fields reflected the correlations between components of individual sensor vectors – i.e., the higher-order signatures of learned odors. Differentiated GCs thereby developed selectivity for particular odor signatures and became unresponsive to other sensory input combinations.

Adult neurogenesis

The process of GC differentiation permanently depleted the pool of interneurons available for recruitment into new odor representations. To avoid a decline in performance as the numbers of odors learned by the network increased, we periodically added new, undifferentiated GC interneurons to the network on a timescale slower than that of the synaptic plasticity rules – a process directly analogous to adult neurogenesis in olfactory bulb^{14, 15, 30, 31, 40}. Specifically, new

networks were constructed with five GCs per column, as described above. After the learning of each new odor, an additional set of five undifferentiated GCs was configured in every column. As with the initial network elements, every MC in the network formed excitatory synapses onto new GCs with a probability of 0.2 (20%), and the new GCs all formed inhibitory synapses onto their cocolumnar MCs with initial inhibitory weights of zero.

Inhibitory synaptic plasticity

In the neuromorphic model, inhibitory synapses from presynaptic GCs onto their cocolumnar MC somata exhibited three functional states. The default state of the synapse was an inactive state I, which exerted no effect on the MC (i.e., equal to 0). When a spike was evoked in the GC, the synapse transitioned into an inhibitory blocking state B; this state was maintained for a period of time Δ_B that was determined by learning. While in this state, the synapse maintained a unit level of inhibition (equal to -1) in the postsynaptic MC soma that inhibited somatic spike propagation. The blocking period Δ_B therefore governed MC spike latency, and corresponded functionally to the inhibitory synaptic weight. At the end of the blocking state, the synapse transitioned to a release state R for 1 timestep, during which it generated a unit level of excitation (equal to +1) in the postsynaptic MC soma. The synapse then resumed the inactive state. An MC soma propagated a spike when the sum of the excitation and inhibition generated by its apical dendrite and by the synapses of all of its presynaptic GCs was positive. After spiking once, the MC soma was refractory to further spiking for the duration of that gamma cycle.

All inhibitory synaptic weights in new GCs were initialized to $\Delta_B = 0$ ts. During training, additionally, the effects of inhibition on MC somata were suppressed. If an MC AD initiated a

spike within the permissive epoch immediately following a cocolumnar GC spike (in the previous inhibitory epoch), the blocking period Δ_B imposed by that GC onto the soma of that MC was modified based on the learning rule

$$\delta_b = \eta(t_{AD} - t_R) \quad (2)$$

where δ_b is the change in the blocking period Δ_B (inhibitory synaptic weight), t_{AD} is the time of the MC spike initiation event in the AD, t_R is the time at which the inhibitory synapse switched from the blocking state to the release state, and η was the learning rate (set to 1.0 for one-shot and 0.25 for ten-shot learning). Consequently, the synaptic blocking period Δ_B was modified during training (rounding up fractions) until the release of inhibition from that synapse was aligned with the spike initiation event in the MC AD (Figure 2c). If the GC spike was not followed by an MC spike initiation event during the following permissive epoch, the inhibitory weight Δ_B of that synapse grew until that MC was inhibited for the entire gamma cycle. Inputs from multiple local GCs onto a common MC were applied and modified independently.

In total, this inhibitory synaptic plasticity rule enabled the EPL network to learn the timing relationships between GC spikes and cocolumnar MC spikes associated with a given odor stimulus, thereby training the inhibitory weight matrix to construct an attractor around the odor representation being learned. This served to counteract the consequences of destructive interference in odor stimuli presented during testing. Importantly, this plasticity rule effectively learned the specific ratiometric patterns of activation levels among MCs that characterized particular odors; consequently, two odors that activated the same population of MCs, but at different relative levels, could be readily distinguished.

Sample occlusion

After training, we tested the network’s performance on recognizing learned odorants in the presence of destructive interference from unpredictable sources of olfactory occlusion. The responses of primary olfactory receptors to a given odorant of interest can be radically altered by the concomitant presence of competing background odorants that strongly activate or block some of the same receptors as the odorant of interest, greatly disrupting the ratiometric activation pattern across receptors on which odor recognition depends. Accordingly, we modeled this occlusion with the highly destructive method of impulse noise. Specifically, an occluded test sample was generated by choosing a fraction P of the 72 elements of a sensor activity vector and replacing them each with random values drawn uniformly from the sensors’ operating range (integer values from 0 to 15). When multiple occluded test samples were generated to measure average performance, both the identities of the occluded elements and the random values to which they were set were redrawn from their respective distributions.

Sample classification

The pattern of MC spikes in each successive gamma cycle was recorded as a set of spikes, with each spike defined by the identity of the active MC and the spike latency with respect to the onset of that permissive epoch. Accordingly, five successive sets of spikes were produced for each sample “sniff”. When an impulse noise-occluded sample was presented to the network, the similarities were computed between each of the five representations evoked by the unknown and each of the network’s learned odor representations. Similarity between two representations was measured with the Jaccard index, defined as the number of spikes in the intersection of two representations, divided by the number of spikes in their union ⁴¹. The occluded sample was

classified as one of the network’s known odorants if the similarity exceeded a threshold of 0.75 in the fifth (final) gamma cycle. If similarities to multiple learned odorants crossed the threshold, the odorant exhibiting the greatest similarity value across the five gamma cycles was picked as the classification result. If none of the similarity values crossed the threshold within five gamma cycles, the odorant was classified as unknown.

Benchmarks

We first compared the classification performance of the EPL network to three conventional signal processing techniques: a median filter (MF), a total variation filter (TVF), and principal component analysis (PCA; Figure 5a) ^{4,54}. The MF used a window size of 5, and was implemented with the Python signal processing library *scipy.signal*. The TVF used a regularization parameter equal to 0.5, and was implemented using the Python image processing library *scikit-image*. PCA was implemented using the Python machine learning library *scikit-learn*; data were projected onto the top five components.

We also compared the performance of the EPL network to a seven-layer deep autoencoder ^{55,56} constructed using the Python deep learning library *Keras*. The seven layers consisted of an input layer of 72 units, followed by five hidden layers of 720 units each and an output layer of 72 units. This resulted in a network of 3744 units, identical to the number in the EPL model when trained with ten odors. The network was fully connected between layers, and the activity of each unit in the hidden layers was L1 regularized. The network was trained with iterative gradient descent until convergence using the Adadelta optimizer with a mean absolute error loss function.

To compare EPL performance with these nonspiking techniques, we used a Manhattan distance metric. Specifically, for each of the techniques, the output was read as a 72-dimensional

vector and normalized such that their elements summed up to a value of unity. The similarity between two such vectors was measured as $(1/(1+d))$ where d is the Manhattan distance between the two vectors. Classification performance was measured by computing this similarity between the output of training data samples and those of test data samples. A test data sample was classified according to the identity of the training data sample to which it was most similar, provided that this similarity value exceeded a threshold of 0.75.

We trained the DAE in three different ways for comparison with EPL network performance. First, the DAE was trained using the same ten non-occluded odor samples that were used to train the EPL model. These ten samples underwent 1000 training epochs to ensure convergence, and were intercalated in presentation so as to minimize interference among different odorant representations (Figure 5a). Second, we trained the DAE to map differently occluded samples of each odorant to a common representation, so as to explicitly learn the full distribution of stimulus variance. Specifically, we trained the DAE on 500 to 7000 training samples, where each sample comprised an independently occluded instance of each of the ten odorants. Each training set was presented for 25 training epochs to ensure convergence. The occlusion levels for each training sample were drawn from the same distribution as the test samples, being randomly and uniformly selected from the range $P = [0.2, 0.8]$. With this procedure, we show that the DAE requires 3000 training samples per odorant to achieve the classification performance that the EPL model achieved with 1 training sample per odorant (Figure 5c); i.e., the EPL model is 3000 times more data efficient than the DAE. Third, we trained the DAE and EPL models first on one odorant (toluene) and then, subsequently, on a second odorant (acetone) in order to compare the models' online learning capabilities. After training on toluene, the DAE classified test presentations of toluene with high fidelity (Figure 5c). However, over the course of acetone

training, the similarity between test samples of toluene and the learned representation of toluene progressively declined (Figure 5c), to the point that the DAE network became unable to correctly classify toluene (Figure 5c; see ³⁹ for strategies to improve the online learning performance of deep networks). In contrast, training the EPL network with acetone exhibited almost no interference with the preexisting toluene representation (Figure 5d, *inset*).

Implementation on the Loihi neuromorphic system

Neuromorphic systems are custom integrated circuits that model biological neural computations, typically with orders of magnitude greater speed and energy efficiency than general-purpose computers. These systems enable the deployment of neural algorithms in edge devices, such as chemosensory signal analyzers, in which real-time operation, low power consumption, environmental robustness, and compact size are critical operational metrics. Loihi, a neuromorphic processor developed for research at Intel Labs, advances the state of the art in neuromorphic systems with innovations in architecture and circuit design, and a feature set that supports a wide variety of neural computations ³². Below we provide an overview of the Loihi system and our network implementation thereon.

Loihi is fabricated in Intel's 14-nm FinFET process and realizes a total of 2.07 billion transistors over a manycore mesh. Each Loihi chip contains a total of 128 neuromorphic cores, along with three embedded Lakemont x86 processors and external communication interfaces that enable the neuromorphic mesh to be extended across many interlinked Loihi chips (Figure 6a). Each neuromorphic core comprises leaky-integrate-and-fire compute units that integrate filtered spike trains from a configurable set of presynaptic units and generate spikes when a threshold level of excitation is crossed. Postsynaptic spikes then are communicated to a configurable set of

target units anywhere within the mesh. A variety of features can be configured in a core, including multicompartment interactions, spike timing-dependent learning rules, axonal conduction delays, and neuromodulatory effects. All signals in the system are digital, and networks operate as discrete-time dynamical systems.

We configured each column of our model within one neuromorphic core, thereby using a total of 72 cores on a single chip. Cocolumnar synaptic interactions took place within a core, whereas the global projections of MC somatic spikes were routed via the intercore routing mesh. The configured network utilized 12.5% of the available neural resources per core and 6% of the available synaptic memory.

Completing one inference cycle (sniff; 5 gamma cycles; 200 timesteps) of the 72-core network required 2.75 ms and consumed 0.43 mJ, of which 0.12 mJ is dynamic energy. Critically, the time required to solution was not significantly affected by the scale of the problem (number of OB columns; Figure 6b), owing to the Loihi architecture’s fine-grained parallelism. This scalability highlights a key advantage of neuromorphic hardware for application to computational neuroscience and machine olfaction. Energy consumption also scaled only modestly as network size increased (Figure 6c), owing to the colocalization of memory and compute and the use of sparse (spiking) communication, which minimize the movement of data. Using multichip Loihi systems, we envision scaling up the present implementation to hundreds of columns and hundreds of thousands of interneurons, as well as to integrate circuit models of the glomerular layer⁵⁷ and the piriform cortex with the current EPL network of olfactory bulb.

References

1. Goff, S.A. & Klee, H.J. Plant volatile compounds: sensory cues for health and nutritional value? *Science* **311**, 815-819 (2006).
2. Araneda, R.C., Kini, A.D. & Firestein, S. The molecular receptive range of an odorant receptor. *Nat Neurosci* **3**, 1248-1255 (2000).
3. Araneda, R.C., Peterlin, Z., Zhang, X., Chesler, A. & Firestein, S. A pharmacological profile of the aldehyde receptor repertoire in rat olfactory epithelium. *J Physiol* **555**, 743-756 (2004).
4. Marco, S. & Gutierrez-Galvez, A. Signal and data processing for machine olfaction and chemical sensing: a review. *IEEE Sensors* **12**, 3189-3214 (2012).
5. Vergara, A., *et al.* On the performance of gas sensor arrays in open sampling systems using Inhibitory Support Vector Machines. *Sens Actuat B* **185**, 462-477 (2013).
6. Marco, S., *et al.* A biomimetic approach to machine olfaction, featuring a very large-scale chemical sensor array and embedded neuro-bio-inspired computation. *Microsystem Technologies (full name of journal)* **20**, 729-742 (2014).
7. Persaud, K.C., Marco, S. & Gutierrez-Galvez, A. *Neuromorphic olfaction* (CRC Press, New York, 2013).
8. Cleland, T.A. Construction of odor representations by olfactory bulb microcircuits. *Prog Brain Res* **208**, 177-203 (2014).
9. Cleland, T.A., Narla, V.A. & Boudadi, K. Multiple learning parameters differentially regulate olfactory generalization. *Behav Neurosci* **123**, 26-35 (2009).
10. Chu, M.W., Li, W.L. & Komiyama, T. Balancing the robustness and efficiency of odor representations during learning. *Neuron* **92**, 174-186 (2016).
11. Doucette, W. & Restrepo, D. Profound context-dependent plasticity of mitral cell responses in olfactory bulb. *PLoS Biol* **6**, e258 (2008).
12. Tong, M.T., Kim, T.P. & Cleland, T.A. Kinase activity in the olfactory bulb is required for odor memory consolidation. *Learn Mem* **25**, 198-205 (2018).
13. Chu, M.W., Li, W.L. & Komiyama, T. Lack of pattern separation in sensory inputs to the olfactory bulb during perceptual learning. *eNeuro* **4** (2017).
14. Sultan, S., *et al.* Learning-dependent neurogenesis in the olfactory bulb determines long-term olfactory memory. *FASEB J* **24**, 2355-2363 (2010).
15. Moreno, M.M., *et al.* Olfactory perceptual learning requires adult neurogenesis. *Proc Natl Acad Sci U S A* **106**, 17980-17985 (2009).
16. Bathellier, B., Lagier, S., Faure, P. & Lledo, P.M. Circuit properties generating gamma oscillations in a network model of the olfactory bulb. *J Neurophysiol* **95**, 2678-2691 (2006).
17. Peace, S.T., *et al.* Coherent olfactory bulb gamma oscillations arise from coupling independent columnar oscillators. *BioRxiv* doi: **10.1101/213827** (2018).

18. Kashiwadani, H., Sasaki, Y.F., Uchida, N. & Mori, K. Synchronized oscillatory discharges of mitral/tufted cells with different molecular receptive ranges in the rabbit olfactory bulb. *J Neurophysiol* **82**, 1786-1792 (1999).
19. Linster, C. & Cleland, T.A. Decorrelation of odor representations via spike timing-dependent plasticity. *Front Comput Neurosci* **4**, 157 (2010).
20. Masquelier, T., Hugues, E., Deco, G. & Thorpe, S.J. Oscillations, phase-of-firing coding, and spike timing-dependent plasticity: an efficient learning scheme. *J Neurosci* **29**, 13484-13493 (2009).
21. Banerjee, A., *et al.* An interglomerular circuit gates glomerular output and implements gain control in the mouse olfactory bulb. *Neuron* **87**, 193-207 (2015).
22. Cleland, T.A., Johnson, B.A., Leon, M. & Linster, C. Relational representation in the olfactory system. *Proc Natl Acad Sci U S A* **104**, 1953-1958 (2007).
23. Cleland, T.A., *et al.* Sequential mechanisms underlying concentration invariance in biological olfaction. *Front Neuroeng* **4**, 21 (2012).
24. Miller, P. Itinerancy between attractor states in neural systems. *Curr Opin Neurobiol* **40**, 14-22 (2016).
25. Gao, Y. & Strowbridge, B.W. Long-term plasticity of excitatory inputs to granule cells in the rat olfactory bulb. *Nat Neurosci* **12**, 731-733 (2009).
26. Lepousez, G., *et al.* Olfactory learning promotes input-specific synaptic plasticity in adult-born neurons. *Proc Natl Acad Sci U S A* **111**, 13984-13989 (2014).
27. de Almeida, L., Idiart, M. & Linster, C. A model of cholinergic modulation in olfactory bulb and piriform cortex. *J Neurophysiol* **109**, 1360-1377 (2013).
28. Devore, S. & Linster, C. Noradrenergic and cholinergic modulation of olfactory bulb sensory processing. *Front Behav Neurosci* **6**, 52 (2012).
29. Li, G., Linster, C. & Cleland, T.A. Functional differentiation of cholinergic and noradrenergic modulation in a biophysical model of olfactory bulb granule cells. *J Neurophysiol* **114**, 3177-3200 (2015).
30. Kermen, F., Sultan, S., Sacquet, J., Mandairon, N. & Didier, A. Consolidation of an olfactory memory trace in the olfactory bulb is required for learning-induced survival of adult-born neurons and long-term memory. *PLoS One* **5**, e12118 (2010).
31. Lepousez, G., Valley, M.T. & Lledo, P.M. The impact of adult neurogenesis on olfactory bulb circuits and computations. *Annu Rev Physiol* **75**, 339-363 (2013).
32. Davies, M., *et al.* Loihi: a neuromorphic manycore processor with on-chip learning. *IEEE Micro* **38**, 82-99 (2018).
33. Li, G. & Cleland, T.A. A coupled-oscillator model of olfactory bulb gamma oscillations. *PLoS Comput Biol* **13**, e1005760 (2017).
34. McIntyre, A.B. & Cleland, T.A. Biophysical constraints on lateral inhibition in the olfactory bulb. *J Neurophysiol* **115**, 2937-2949 (2016).

35. Lagier, S., *et al.* GABAergic inhibition at dendrodendritic synapses tunes gamma oscillations in the olfactory bulb. *Proc Natl Acad Sci U S A* **104**, 7259-7264 (2007).
36. McTavish, T.S., Migliore, M., Shepherd, G.M. & Hines, M.L. Mitral cell spike synchrony modulated by dendrodendritic synapse location. *Front Comput Neurosci* **6**, 3 (2012).
37. Borthakur, A. & Cleland, T.A. A neuromorphic transfer learning algorithm for orthogonalizing highly overlapping sensor array responses. in *ISOCS/IEEE International Symposium on Olfaction and Electronic Nose (ISOEN)* 1-3 (Montreal, QC, Canada, 2017).
38. French, R.M. Catastrophic forgetting in connectionist networks. *Trends Cogn Sci* **3**, 128-135 (1999).
39. Kirkpatrick, J., *et al.* Overcoming catastrophic forgetting in neural networks. *Proc Natl Acad Sci U S A* **114**, 3521-3526 (2017).
40. Chow, S.F., Wick, S.D. & Riecke, H. Neurogenesis drives stimulus decorrelation in a model of the olfactory bulb. *PLoS Comput Biol* **8**, e1002398 (2012).
41. Levandowsky, M. & Winter, D. Distance between sets. *Nature* **234**, 34-35 (1971).
42. Moreno, M.M., *et al.* Action of the noradrenergic system on adult-born cells is required for olfactory learning in mice. *J Neurosci* **32**, 3748-3758 (2012).
43. Hasselmo, M.E. & Giocomo, L.M. Cholinergic modulation of cortical function. *J Mol Neurosci* **30**, 133-135 (2006).
44. Mandairon, N., *et al.* Cholinergic modulation in the olfactory bulb influences spontaneous olfactory discrimination in adult rats. *Eur J Neurosci* **24**, 3234-3244 (2006).
45. Mandairon, N., *et al.* Context-driven activation of odor representations in the absence of olfactory stimuli in the olfactory bulb and piriform cortex. *Front Behav Neurosci* **8**, 138 (2014).
46. Strowbridge, B.W. Role of cortical feedback in regulating inhibitory microcircuits. *Ann N Y Acad Sci* **1170**, 270-274 (2009).
47. Thorpe, S., Delorme, A. & Van Rullen, R. Spike-based strategies for rapid processing. *Neural Netw* **14**, 715-725 (2001).
48. Hopfield, J.J. Pattern recognition computation using action potential timing for stimulus representation. *Nature* **376**, 33-36 (1995).
49. Izhikevich, E.M. Polychronization: computation with spikes. *Neural Comput* **18**, 245-282 (2006).
50. Maass, W. Paradigms for computing with spiking neurons. in *Models of Neural Networks IV. Physics of Neural Networks* (ed. J.L. van Hemmen, J.D. Cowan & E. Domany) 373-402 (Springer, New York, 2002).
51. Maass, W. & Markram, H. On the computational power of circuits of spiking neurons. *J Comput Sys Sci* **69**, 593-616 (2004).
52. Luna, V.M. & Schoppa, N.E. GABAergic circuits control input-spike coupling in the piriform cortex. *J Neurosci* **28**, 8851-8859 (2008).
53. Feldman, D.E. The spike-timing dependence of plasticity. *Neuron* **75**, 556-571 (2012).

54. Huang, Y.-M., Ng, M.K. & Wen, Y.-W. Fast image restoration methods for impulse and Gaussian noises removal. *IEEE Sig Proc Lett* **16**, 457-460 (2009).
55. Hinton, G.E. & Salakhutdinov, R.R. Reducing the dimensionality of data with neural networks. *Science* **313**, 504-507 (2006).
56. Xie, J., Xu, L. & Chen, E. Image denoising and inpainting with deep neural networks. in *Proceedings of the 25th International Conference on Neural Information Processing Systems* 341-349 (Lake Tahoe, NV, 2012).
57. Imam, N., *et al.* Implementation of olfactory bulb glomerular-layer computations in a digital neurosynaptic core. *Front Neurosci* **6**, 83 (2012).

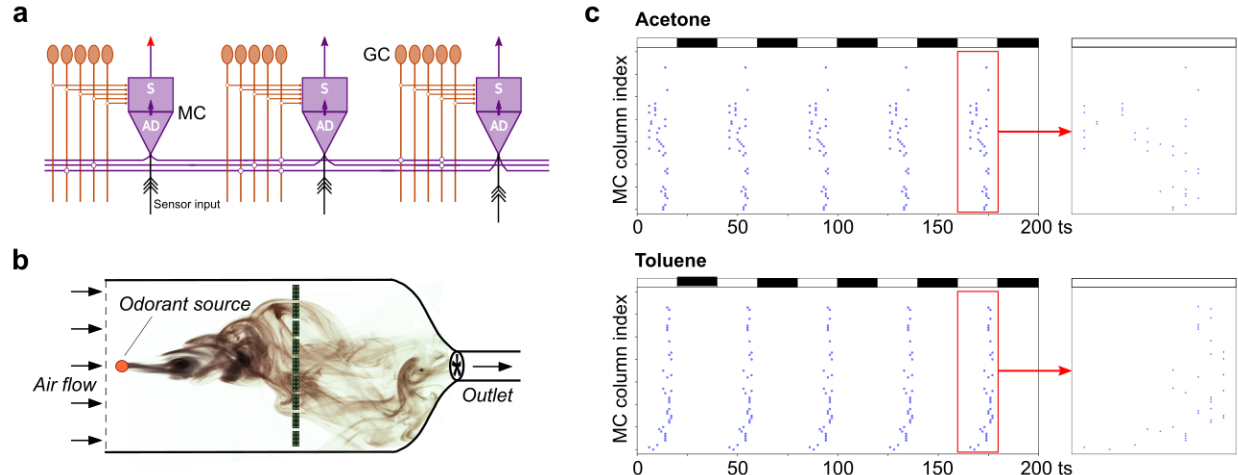


Figure 1. Model structure and signal encoding. **a**, Architecture of the neuromorphic model.

Sensor input is delivered to the apical dendrite (AD) of each mitral cell (MC), which in turn excites its corresponding soma (S). The resulting MC activation is propagated out via its lateral dendrites (*purple*) to synaptically excite the dendrites of granule cells (GC, *orange*). The distribution of excitatory connections (*open circles*) is sparse and independent of spatial proximity. In contrast, GC spiking activity is delivered as inhibition onto its local, cocolumnar MC. **b**, Illustration of odorant delivery to a 72-element chemosensor array within a wind tunnel⁵. Nine banks of eight sensors each were deployed across the full 1.2 m breadth of the tunnel. **c**, Presentation of acetone (*top*) or toluene (*bottom*) to the chemosensor array resulted in characteristic patterns of spiking activity across the 72 MCs (*ordinate*). Stronger sensor activation led to correspondingly earlier MC spikes within each gamma cycle. In the absence of noise, the response was odor-specific but stationary across five sequential gamma cycles. Inhibitory epochs (20 timesteps duration) are denoted by black bars; permissive epochs (20 timesteps) are denoted by white bars. The fifth gamma cycle is expanded in time (*rightmost panels*) to illustrate the distribution of MC spike times. *ts*, timesteps.

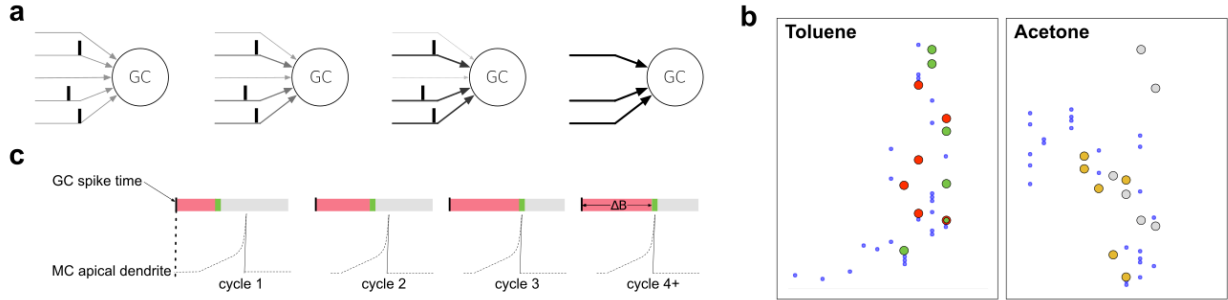


Figure 2. Plasticity rules. **a**, During training, repeated coincident MC spikes converging onto a given GC activated that GC, and developed strong excitatory synaptic weights thereon, whereas other inputs to that GC were weakened and ultimately eliminated. **b**, Excitatory plasticity rendered GCs selective to higher-order features of odor representations. After training on toluene (*left panel*) or acetone (*right panel*), a number of GCs became responsive to specific combinations of activated MCs. Spike times highlighted with *green* spots denote those MC spikes that activated a specific GC in a network trained on toluene. *Red* spots denote a second such GC, responsive to toluene via a different set of activated MCs. *Yellow* and *grey* spots denote analogous MC spike populations that activate two GCs responsive to acetone in the same network. **c**, Illustration of the inhibitory plasticity rule. During training, the weight (duration) of spike-mediated GC inhibition onto its cocolumnar MC (*red bar*) increased until the release of this inhibition (*green*) coincided with spike initiation in the MC apical dendrite. The learned inhibitory weight corresponded to a blocking period ΔB during which spike propagation in the MC soma was suppressed.

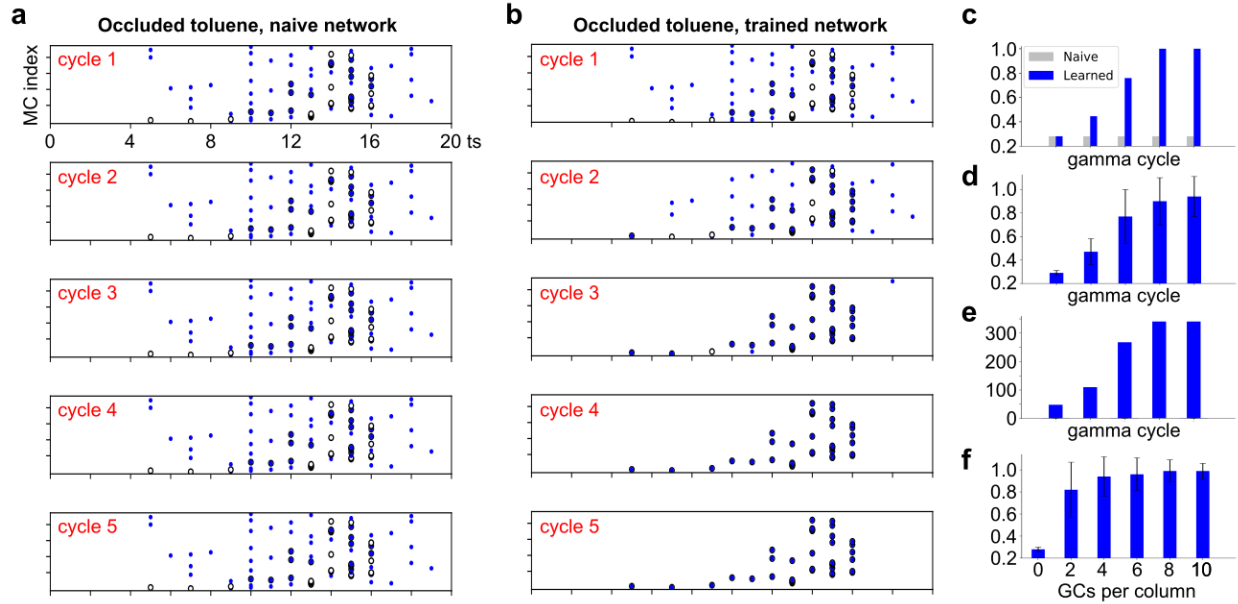


Figure 3. Odorant-evoked MC activity patterns are attracted to learned representations. **a**, Presentation of an occluded instance of toluene to an untrained network. Blue dot rasters denote spike times evoked by occluded toluene (impulse noise $P = 0.6$). The untrained network does not update the response to occluded toluene over the five gamma cycles depicted. For comparison, open circle rasters denote the spike times evoked by non-occluded toluene. ts , timesteps. **b**, Presentation of the same occluded instance of toluene to a network trained on (non-occluded) toluene. The activity profile evoked by the occluded sample was attracted to the learned toluene representation over successive gamma cycles. **c**, The Jaccard similarity⁴¹ between the response to occluded toluene and the learned representation of toluene systematically increased over five gamma cycles in the trained network (panel A), but not in the untrained network (panel B). **d**, The Jaccard similarity increased over five gamma cycles when averaged over 100 independently generated instances of occluded toluene (impulse noise $P =$

0.6). Error bars denote standard deviation. *e*, During learning, the number of GCs tuned to toluene increased over the five successive gamma cycles of training. *f*, Mean Jaccard similarity in the fifth gamma cycle as a function of the number of undifferentiated GCs per column. Mean similarity is averaged across 100 occluded instances of toluene (impulse noise $P = 0.6$); error bars denote standard deviation. Five GCs per column were utilized for all other simulations described herein.

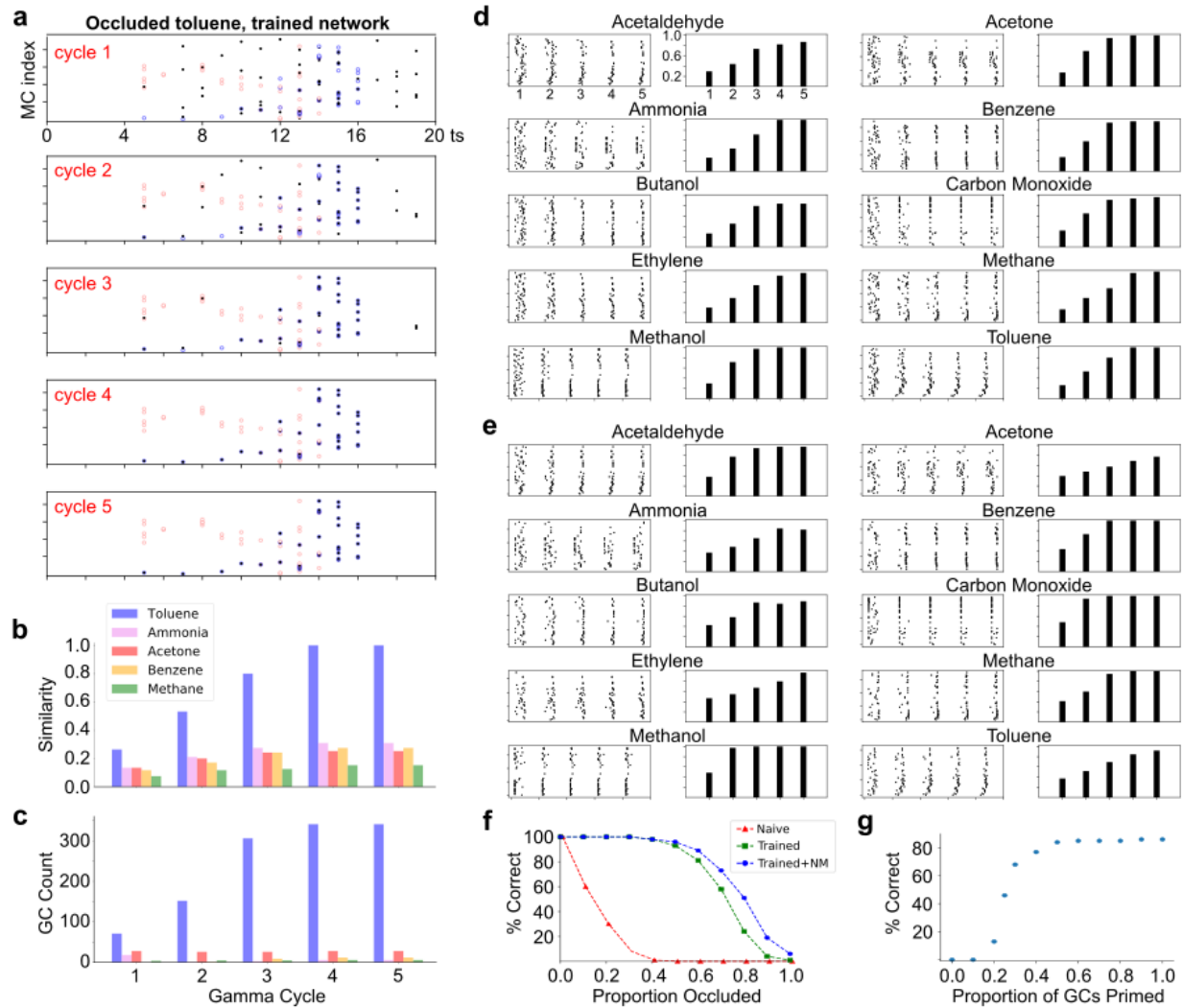


Figure 4. Odor learning. **a**, Spike raster plot depicting attractor dynamics after training the network on all ten odorants. The representation generated by a sample of occluded toluene ($P = 0.6$; black dots) was progressively drawn towards the learned representation of toluene (open blue circles) and away from the learned representations of acetone (open red circles) and the other eight odorants (not shown). *ts*, timesteps. **b**, The Jaccard similarity to toluene that was evoked by the occluded-toluene stimulus increased over five successive gamma cycles until the stimulus was classified as toluene (similarity > 0.8). For clarity, only five odorants are depicted.

c, The number of toluene-tuned GCs activated by the occluded-toluene stimulus progressively increased over five gamma cycles as the MC spiking activity pattern was attracted towards the learned toluene representation. GCs tuned to the other nine odorants were negligibly recruited by the evolving stimulus representation. **d**, Network activity evoked by presentation of occluded instances of each of the ten learned odors following one-shot learning. *Left panels*, spike raster plots over five gamma cycles (200 timesteps); *ordinate* denotes MC index. Right panel, Jaccard similarity between the activity pattern generated by each occluded odorant stimulus and the learned representation of the corresponding odorant. The same network can reliably recognize all ten odorants from substantially occluded examples ($P = 0.6$). **e**, As panel D, but following ten-shot learning of each odorant. **f**, Mean classification performance across all ten odorants under increasing levels of sensory occlusion. The abscissa denotes the level of impulse noise – i.e., the proportion of MC inputs for which the sensory activation level was replaced with a random value. *Red curve*, proportion of correct classifications by an untrained network. *Green curve*, proportion of correct classifications by a network trained on all ten odorants. *Blue curve*, proportion of correct classifications by a trained network with the aid of a neuromodulation-dependent dynamic state trajectory. **g**, Effects of GC priming on classification performance under extreme occlusion. One hundred independently generated samples of occluded toluene with impulse noise $P = 0.9$ were presented to the fully-trained network. The putative effects of priming arising from piriform cortical projections onto bulbar GCs were modeled by lowering the spike thresholds of a fraction of toluene-tuned GCs. As the fraction of toluene-tuned GCs so activated was increased, classification performance increased from near zero to over 80% correct.

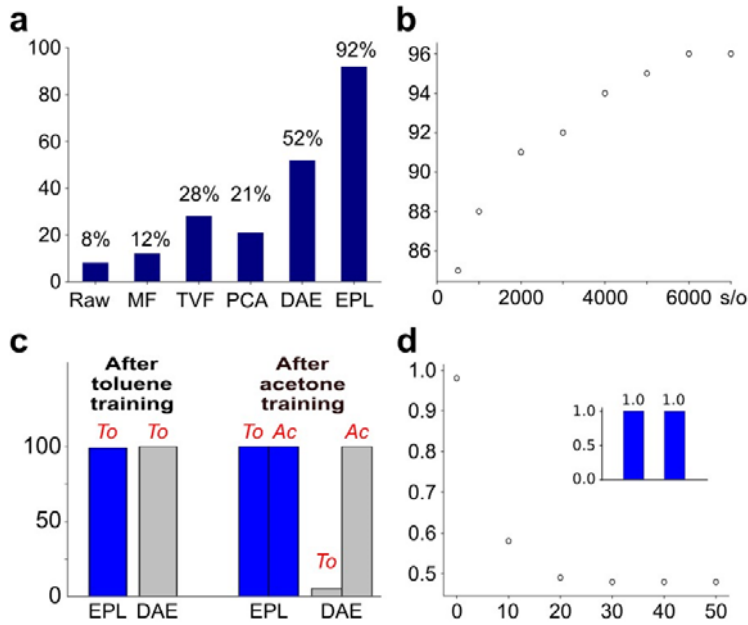


Figure 5. Performance evaluation. **a**, Classification performance of the EPL network in comparison to four other signal processing techniques. *Raw*, classification of unprocessed sensor signals. *MF*, median filter. *TVF*, total variation filter. *PCA*, principal components analysis. *DAE*, a seven-layer deep autoencoder. *EPL*, the neuromorphic EPL model. **b**, The performance of the DAE improved when it was explicitly trained to map a variety of occluded instances of each odor to a common representation. To achieve performance superior to the EPL network with one-shot learning (five gamma cycles), the DAE required 3000 occluded training samples per odor. *Abscissa*, number of training samples per odorant (*s/o*). *Ordinate*, classification performance (%). **c**, Online learning. After training naïve EPL and DAE networks with toluene, both recognized toluene with 100% accuracy. After then training the same network with acetone, the DAE learned to recognize acetone with 100% accuracy, but was no longer able to

recognize toluene (catastrophic forgetting). In contrast, the EPL network retained the ability to recognize toluene after subsequent training on acetone. ***d***, Gradual loss of the toluene representation in the DAE during subsequent training with acetone. The ordinate denotes the similarity of the toluene-evoked activity pattern to the original toluene representation as a function of the number of training trials for acetone. Values are the means of 100 test samples.

Inset, Similarity between the toluene-evoked activity pattern and the original toluene representation in the EPL network before training with acetone (left) and after the completion of acetone training (right).

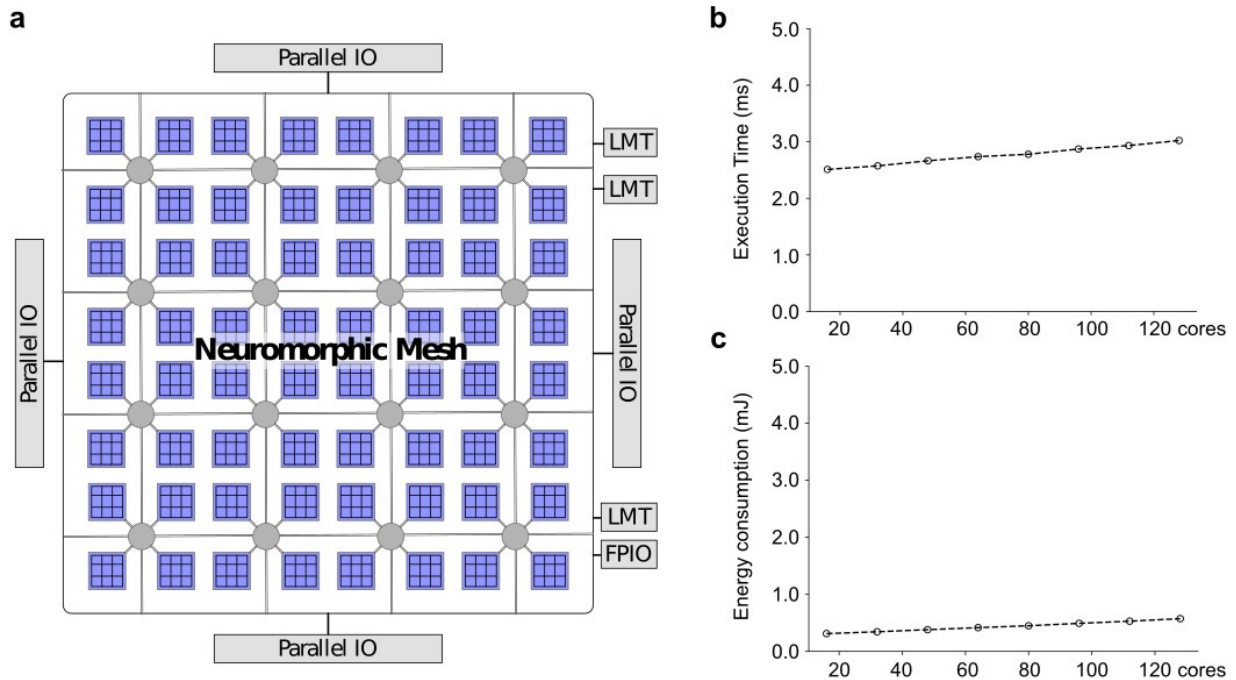


Figure 6. Loihi performance. **a**, The Intel Loihi neuromorphic chip architecture. Neuromorphic cores (blue squares) operate in parallel and communicate through a mesh of spike routers (grey circles). Also depicted are the three embedded x86 Lakemont cores (LMT) and the input/output interfaces (IO). **b**, The execution time to solution is not significantly affected as the EPL network size is expanded. In the present implementation, one Loihi core corresponds to one OB column. **c**, The total energy consumed increases only modestly as the EPL network size is expanded.